International Journal of Mechanical Sciences 100 (2015) 99–111

Contents lists available at ScienceDirect

International Journal of Mechanical Sciences

journal homepage: www.elsevier.com/locate/ijmecsci

Damage evaluation in tube spinnability test with ductile fracture criteria

Hao Ma [a], Wenchen Xu [a,1], Bo Cheng Jin [b], Debin Shan [a,*,1], Steven R. Nutt [b]

[a] School of Materials Science and Engineering & National Key Laboratory for Precision Hot Processing of Metals, Harbin Institute of Technology, Harbin 150001, PR China
[b] M.C. Gill Composites Center, Department of Chemical Engineering and Materials Science, University of Southern California, LA, USA

ARTICLE INFO

Article history:
Received 9 December 2014
Received in revised form
9 May 2015
Accepted 5 June 2015
Available online 12 June 2015

Keywords:
Ductile fracture criteria
Damage
Spinnability
Damage limit

ABSTRACT

Spinnability, the maximum thickness reduction ratio a material can undergo without fracture, has important effects on product quality and production efficiency in tube spinning. However, predicting the rupture limit and spinnability poses challenges due to the complexity of tube spinning process. This study aims to select appropriate ductile fracture criteria (DFCs) in terms of the damage limits, which were obtained by mechanical tests, to accurately predict the forming limit and damage evolution in the tube spinnability test. The periodic stress triaxiality and periodic Lode parameter were firstly introduced by considering the periodical changes of the stress and strain components in the spinning process. Based on the evolution of the two parameters, the out layer of TA2 titanium tube exhibited a higher damage potential, which was consistent with the experiment results. Nine ductile fracture criteria were incorporated into the finite element software (ABAQUS) to simulate the damage evolution in tube spinnability tests. The results show that, except for the Freudenthal, R–T and Ayada models, all of the other ductile fracture criteria are suitable for predicting the damage distribution on TA2 titanium tubes in spinnability tests. The variation of stress triaxiality under different cut-off values in tensile test were much closer to that in spinnability test relative to upsetting test throughout the entire forming process, which led to higher prediction accuracy of the spinnability by the tensile test. For all of the DFCs considered, the C–L criterion provides the most accurate predictions on the spinnability of TA2 titanium tubes.

1. Introduction

Tube spinning is a successively and locally plastic deformation process widely used in industry due to its special advantages, such as simple tooling, reduced loading, higher quality and cost savings. In particular, it is an effective way to manufacture large-diameter thin-walled tubular workpieces [1–4]. In tube spinning, there are two primary failure modes restricting the spinning process and influencing the forming quality of as-spun tubular workpieces, which are plastic flow instability (such as pileup, waviness or bulges [5]) and ductile fracture. Over the years, FE simulation and process experiments have been conducted to reveal the mechanism of flow instability or establish a balance of process variables to achieve suitable flow in tube spinning [6–8], whereas the research works on ductile fracture are limited and most of them are experimental. Early work in this area was performed by Kalpakcioglu [9], who proposed a model to test tube spinnability. For multi-pass spinning process, material spinnability can be used as the basis for predicting the number of spinning passes and the thickness reduction rate of each pass, thus increasing production efficiency and improving product quality. However, the experimental methods for measuring spinnability are complicated by difficulties in determining damage evolution in the forming process.

Ductile fracture criteria (DFCs) have been proposed and applied to the analysis of ductile fractures. For example, the coupling of DFCs with finite element (FE) simulation was used to predict crack initiation, propagation, and final rupture during metal forming. Compared with the forming limit diagram (FLD), which is based on necking models [10–15], damage models based on DFC/FE have distinct advantages in predicting rupture during the spinning process. On the one hand, the three-dimensional body element has been widely used in modeling spinning process, while the FLD method can only be applied to finite elements with plane stress states. On the other hand, the strain path during the spinning process usually deviates from linearity due to complex geometrical, material and boundary conditions. In this case, only DFCs can take into account the nonlinear stress and strain histories in

* Corresponding author.
E-mail addresses: xuwc_76@hit.edu.cn (W. Xu), d.b.shan@gmail.com (D. Shan).
[1] Tel./fax: +86 451 86418732.

http://dx.doi.org/10.1016/j.ijmecsci.2015.06.005
0020-7403/

plastic deformation. However, the applications of DFCs to metal spinning are limited, mainly confined to splitting and shear spinning processes up to now [16], while simulation and damage analysis of the tube spinnability test has not been reported.

In this study, nine ductile fracture criteria were coupled into FEA software (ABAQUS) to simulate the process of crack initiation, propagation and rupture during tube spinning of TA2 titanium, and the spinnability of TA2 titanium tube was predicted using these damage models with tensile and upsetting tests. The applicability of these criteria was evaluated in terms of the ductile fracture location at fracture moment in different samples. In the spinnability test, two important parameters, the periodic stress triaxiality and periodic Lode parameter were introduced firstly to reveal the causes of the failure occurring on TA2 titanium tube. Furthermore, the deformation characteristics (modes) in the tensile, upsetting and tube spinnability tests were analyzed and compared, and the accuracy of selected damage models was verified by spinning experiments.

2. Ductile fracture criteria (DFCs)

In view of the relationship between theoretical models and material responses, the ductile fracture criteria can be classified into two groups. The first group, commonly known as coupled ductile fracture criterion, incorporates damage accumulation into the constitutive equations. By considering the cumulative processes of nucleation, growth and coalescence of voids, a coupled ductile fracture model was proposed by Gurson [17], and further modified by Tvergaard and Needleman [18], now known as the GTN model. Thereafter, some Gurson-type fracture models ([19], [20], [21]) have been developed, which can be used to predict fracture behavior under shear loading. However, these ductile fracture models do not work well for uniaxial compression, plane strain compression and tube spinning [22,23]. In the field of continuum damage mechanics (CDM), another type of coupled ductile fracture model was put forward by Lemaitre [24]. Note that plastic deformation localization is usually neglected in this case, and the CDM model does not accurately predict damage evolution under certain loading conditions, such as uniaxial tension [25].

The second group, usually referred to as uncoupled ductile fracture criteria, neglects the influence of damage on the yield surface. In the uncoupled DFC group, damage accumulation is formulated empirically or on the basis of microscopic mechanisms and various hypotheses. Compared to the complex coupled DFCs, these uncoupled models have been widely used in industry due to the inherent simplicity and the limited number of parameters to be evaluated experimentally. The energy criterion was firstly proposed by Freudenthal [26], who postulated that ductile fracture was dominated by a critical value of the total plastic work per unit volume. Based on the observation that ductile fracture tends to initiate in the region of maximum principal tensile stress, Cockcroft and Latham [27] developed an empirical energetic damage criterion. Oh et al. [28] modified the Cockcroft–Latham criterion by normalizing the first principal tensile stress with the equivalent stress. Brozzo et al. [29] empirically modified the C–L criterion to explicitly consider the effect of the mean stress on the equivalent plastic strain. McClintock [30] proposed a ductile fracture criterion based on analytical formulation of growth of cylindrical and spherical voids under the remotely applied plain strain fields. Rice and Tracey [31] introduced a function to describe the void growth in various stress states by analyzing the growth of a single spherical void in an infinite solid. They concluded that void growth was mainly controlled by the stress triaxiality, defined as the ratio of hydrostatic pressure to the Von Mises equivalent stress. Ayada [32] also used this parameter for ductile fracture, while Bao and Wierzbicki [33] reported that fracture never occurred when stress triaxiality was below the critical value of $-1/3$. In our research, we coupled the critical value of $-1/3$ into the Adaya model to evaluate the applicability for tube spinnability testing. LeRoy et al. [34] proposed a ductile fracture model by considering nucleation, shape change and coalescence of voids in the Rice and Tracey model. In our work, we primarily considered uncoupled DFCs in the tube spinnability test, as shown in Table 1.

Table 1
Brief summary of selected typical uncoupled DFCs.

Criterion	Formula
Freudenthal	$\int_0^{\overline{\varepsilon}_f^p} \overline{\sigma}\, d\overline{\varepsilon}^p = c_1$
Cockcroft and Latham (C–L)	$\int_0^{\overline{\varepsilon}_f^p} \sigma_1\, d\overline{\varepsilon}^p = c_2$
Oh et al. (Oh)	$\int_0^{\overline{\varepsilon}_f^p} \frac{\sigma_1}{\overline{\sigma}} d\overline{\varepsilon}^p = c_3$
Brozzo et al. (Brozzo)	$\int_0^{\overline{\varepsilon}_f^p} \frac{2\sigma_1}{3(\sigma_1-\sigma_m)} d\overline{\varepsilon}^p = c_4$
McClintock	$\int_0^{\overline{\varepsilon}_f^p} \left[\frac{\sqrt{3}}{2(1-n)} \sinh\left\{\frac{\sqrt{3}}{2(1-n)} \frac{\sigma_1+\sigma_2}{\overline{\sigma}}\right\} + \frac{3}{4}\frac{\sigma_1-\sigma_2}{\overline{\sigma}}\right] d\overline{\varepsilon}^p = c_5$
Rice and Tracey (R–T)	$\int_0^{\overline{\varepsilon}_f^p} \exp\left(\frac{3\sigma_m}{2\overline{\sigma}}\right) d\overline{\varepsilon}^p = c_6$
Ayada	$\int_0^{\overline{\varepsilon}_f^p} \frac{\sigma_m}{\overline{\sigma}} d\overline{\varepsilon}^p = c_7$
LeRoy et al. (LeRoy)	$\int_0^{\overline{\varepsilon}_f^p} (\sigma_1 - \sigma_m)\, d\overline{\varepsilon}^p = c_9$

where $\overline{\varepsilon}_f^p$ is the fracture plastic strain, $\overline{\varepsilon}^p$ is the equivalent plastic strain, σ_1 is the first principal tensile stress, σ_2 is the second principal tensile stress, $\overline{\sigma}$ is the Von Mises equivalent stress, σ_m is the mean (hydrostatic) stress, n is the hardening exponent, c_1–c_9 are the damage limits.

3. Experiment results

3.1. Tensile and upsetting test

Tensile and upsetting tests were performed using an INSTRON 1186 testing machine with a 100 kN load cell. The gauge length is 12.5 mm for the tensile test, and the dimension is $\Phi 5\ \text{mm} \times 7.5\ \text{mm}$ for the upsetting test, as shown in Fig. 1. In the tensile test, the sudden drop in the load magnitude during loading was identified as the moment of fracture. As the deformation progressed, localization (necking or instability) initiated in the necking zone and further developed to ductile fracture. In the upsetting test, the same dimensional specimens were compressed to different stages in order to capture the fracture initiation more accurately. Because of friction between specimens and flat indenter, a barreling effect occurred near the equator of the specimen, leading to the development of circumferential tensile stresses and therefore initiation of crack failure.

3.2. Experiment of spinnability test

Kalpakcioglu proposed a method for testing the spinnability of materials in tube spinning [9]. In this method, the rollers move along the trajectory at a small angle φ to the generatrix of the

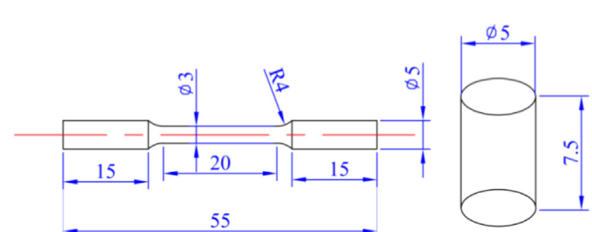

Fig. 1. The sample size for the tensile and upsetting tests.

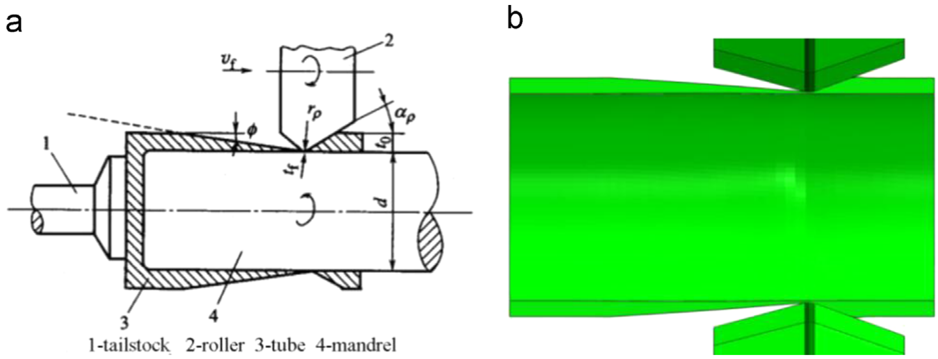

Fig. 2. Tube spinnability test: (a) schematic diagram; (b) deformed shape of simulation results.

mandrel, so the thickness can be reduced continuously from t_0 to t_f, as shown in Fig. 2.

Fig. 3 shows the photographs of TA2 titanium as-spun tubes in the spinnability test. The spinning experiments were conducted in linear trajectories with wedge angles of 2°, 3° and 4°, respectively. The die and process parameters of the spinnability test are shown in Table 2. When the thinning rate increased to 64.6% using a trajectory with 4° wedge angle, no macroscopic crack was observed in the as-spun tube, as shown in Fig. 3a. Failure was initiated at the outer surface as the thinning rate reached 66.1%, and developed with a macroscopic circumferential fracture with the thinning rate of 66.9%, as shown in Fig. 3b and Fig. 7c. Similar circumferential fractures were observed in as-spun tubes using other wedge angles, as shown in Fig. 3d and e. The spinnability obtained by such tests is summarized in Table 3.

Table 2
Die and process parameters of tube spinnability test.

Parameters	Value
Diameter of mandrel d (mm)	65
Forming angle α_ρ (°)	20
Fillet radius of roller r_ρ (mm)	6
Initial thickness of tube t_0 (mm)	5
Feed radio f (mm/r)	0.7
Wedge Angle φ (°)	2, 3, 4

Table 3
Spinnability obtained by the experiment of tube spinnability test.

Wedge angle φ(°)	2°	3°	4°
Spinnability	71.2%	69.5%	66.1%

4. Damage prediction

4.1. FE simulation model

FE models were established in the ABAQUS/Explicit platform to simulate the spinning process. The material of the deformable body was assumed to be homogeneous and isotropic. An isotropic power hardening law was used to model the plastic behavior of TA2 titanium, expressed as $\sigma = 869.2022(0.09208+\varepsilon)^{0.12}$. The tube blank was modeled with 3D 8-node brick elements with reduced integration (C3D8R). The penalty contact method was adopted to simulate the contact between the material and tools, and Coulomb's friction law was selected to model the sliding behavior between them.

4.2. Evaluation of the DFCs

In the uncoupled DFC category, damage accumulation is generally formulated with the general function in Eq. (2). As the forming process proceeds into the fracture stage, the damage accumulation reaches the damage limit at the critical location where failure is initiated

$$\int_0^{\bar{\varepsilon}_f^p} (\sigma, \bar{\varepsilon}^p) d\bar{\varepsilon}^p = c \tag{1}$$

In the present study, the critical material point was located in the center region of the necking zone for tensile tests, while it was located in the central equatorial region for upsetting tests, as discussed in Section 3.1. For tube spinnability tests, the outer surface with the greatest thickness reduction was the critical location, as observed in Section 3.2.

The applicability of DFCs is evaluated in this section in terms of the location of ductile fracture at the moment of fracture. In tensile tests, the maximum damage appeared in the center of the specimen (critical material point), as shown in Fig. 4. All of the ductile fracture criteria yielded accurate predictions of fracture initialization and location due to necking deformation. In particular, localized deformation enabled the damage models to accurately capture failure initiation.

The fracture initialization and location predicted using the selected criteria in the upsetting test are shown in Fig. 5. In the upsetting test, failure was initiated at the sample equator and developed with an inclined fracture surface. This kind of shear fracture was attributed to the distribution of closest packed slip planes of the material, an explanation first proposed by Bao [35], unlike the damage accumulation induced by nucleation, growth, and coalescence of voids. Recently, this mechanism was quoted by Khan and Liu [25]. Images of the fracture surface of the TA2 titanium upsetting specimen exhibited similar features, as shown in Fig. 6. In addition, the DFCs based on micro-void analysis (e.g., models of McClintock, R–T, and LeRoy), did not accurately predict the location of the maximum damage in compression, nor did the Freudenthal model. Similarly, Bao [35] stated that the models of McClintock, R–T, and LeRoy were not suitable for predicting the fracture behavior in compression test. Li et al. [23] reported that the R–T model yielded inaccurate damage prediction for upsetting tests. Generally, the damage increased with increasing plastic deformation, but the Ayada model yielded unrealistic damage values (less than zero) in the deformed billet, indicating it was not suitable for upsetting test. Only the C–L, Oh, Brozzo, and modified Ayada (Ayada-m) models yielded accurate predictions of the damage location in upsetting billets in the present evaluation.

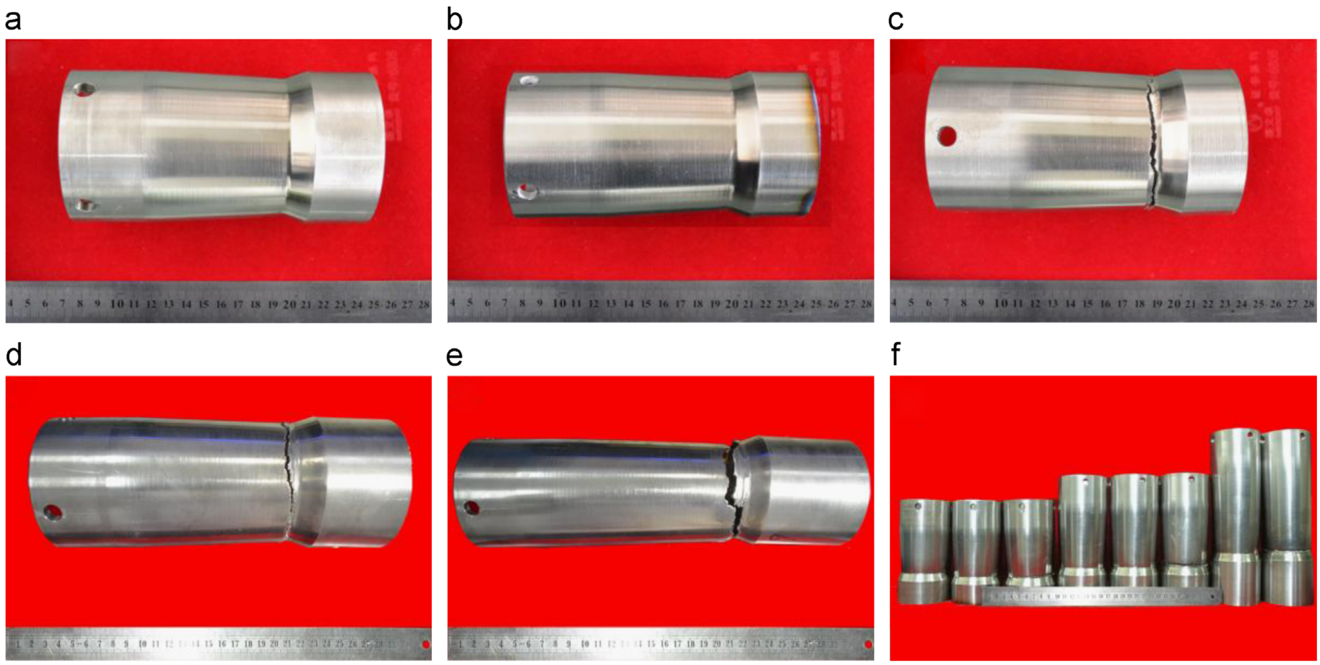

Fig. 3. Photographs of TA2 titanium as-spun tubes in spinnability test: (a) uncracked tube under 4° wedge angle; (b) tube with crack initiation under 4° wedge angle; (c) circumferential cracked tube under 4° wedge angle; (d) circumferential cracked tube under 3° wedge angle; (e) circumferential cracked tube under 2° wedge angle; (f) tubes with different thinning rates and wedge angles.

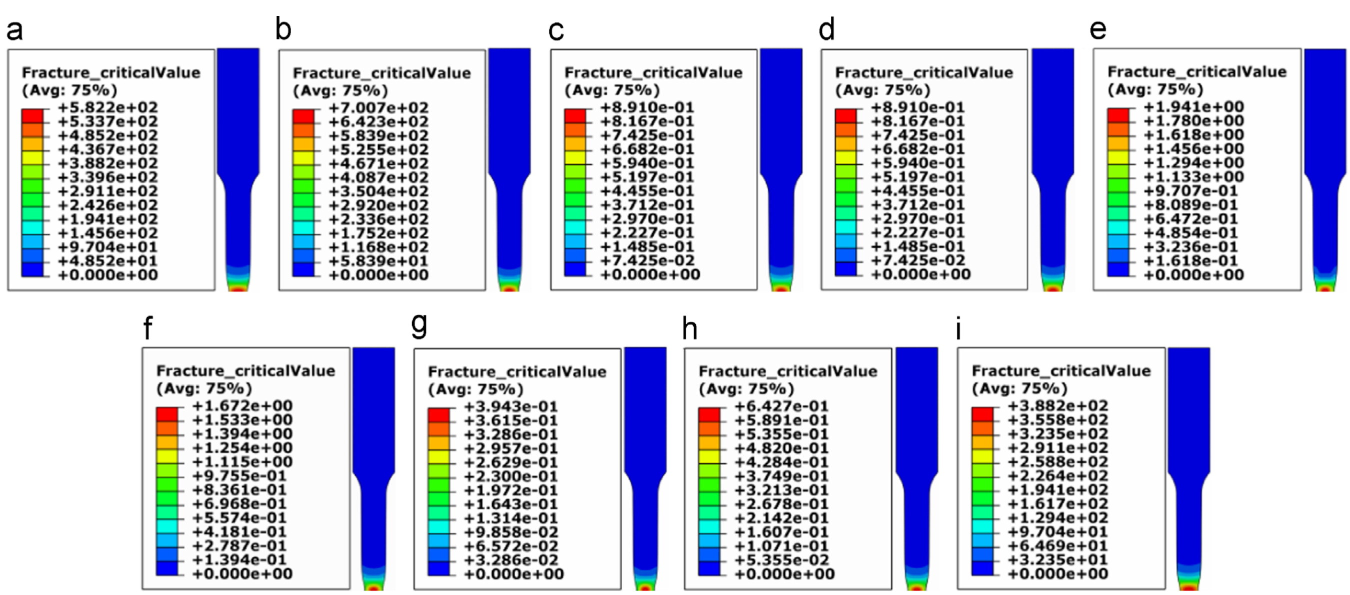

Fig. 4. Distributions of the damage values in the tensile test with different criteria at fracture moment: (a) Freudenthal model; (b) C–L model; (c) Oh model; (d) Brozzo model; (e) McClintock model; (f) R–T model; (g) Ayada model; (h) Ayada-m model; (i) LeRoy model.

4.3. Damage distribution and evaluation of tube spinnability test

The initialization and location of fracture predicted by the selected criteria in the spinnability test are shown in Fig. 7. Except for the Ayada model, all of the ductile fracture criteria yielded predictions of the circumferential crack in TA2 tubes. In addition, with the exception of the Freudenthal model, the maximum damage appeared in the outer layer at the fracture location, as shown in Fig. 8. Both simulation results and experimental observations indicated that the crack initiated in the outer layer and developed a circumferential crack with increasing thinning rate, as discussed in Section 3.2. In summary, the Ayada and Freudenthal models did not predict the circumferential crack on outer surface of TA2 titanium tubes in spinnability tests. Thus, we henceforth limit our discussion to the remaining ductile fracture criteria.

To further investigate damage evolution in the spinnability test, five paths were established along the axial direction from the starting point to the free end. Path1–path5 represent 5 node sets from the outer layer to the inner layer, respectively. Except for the R–T model, the damage evaluation predicted by other DFCs were similar to the C–L model. Thus, only C–L and R–T models are discussed in this section, as shown in Figs. 9 and 10.

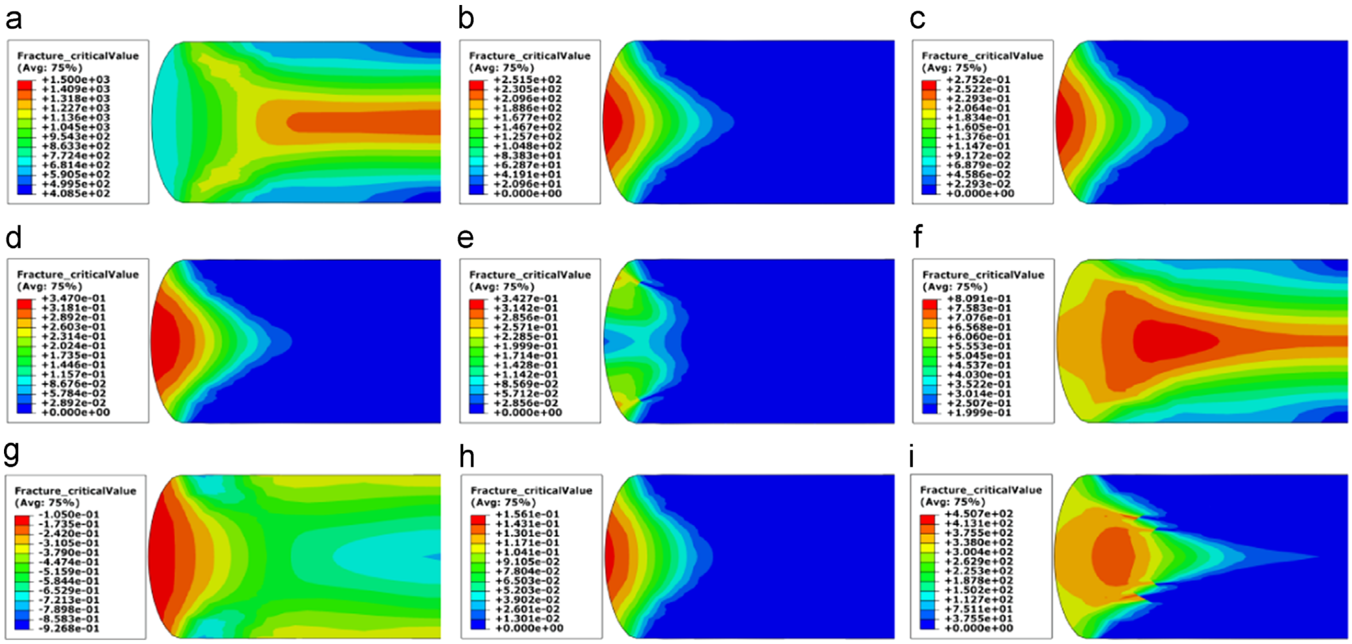

Fig. 5. Distributions of the damage values in the upsetting test with different criteria at fracture moment: (a) Freudenthal model; (b) C–L model; (c) Oh model; (d) Brozzo model; (e) McClintock model; (f) R–T model; (g) Ayada model; (h) Ayada-m model; (i) LeRoy model.

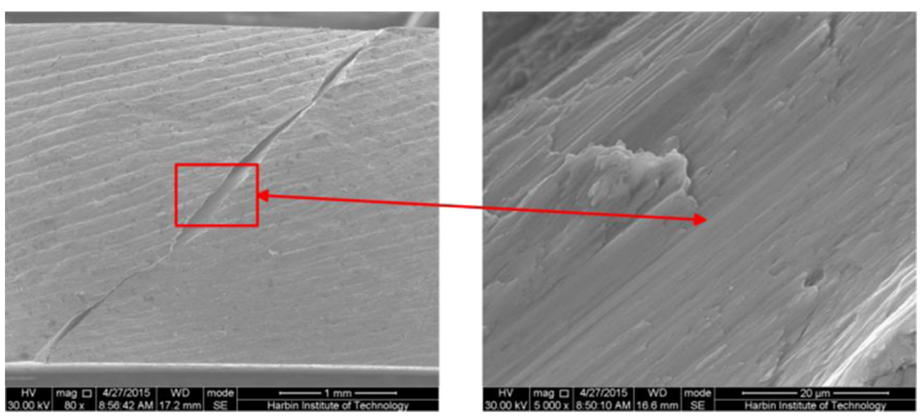

Fig. 6. Fractograph showing flat fracture surface in the TA2 titanium upsetting specimen.

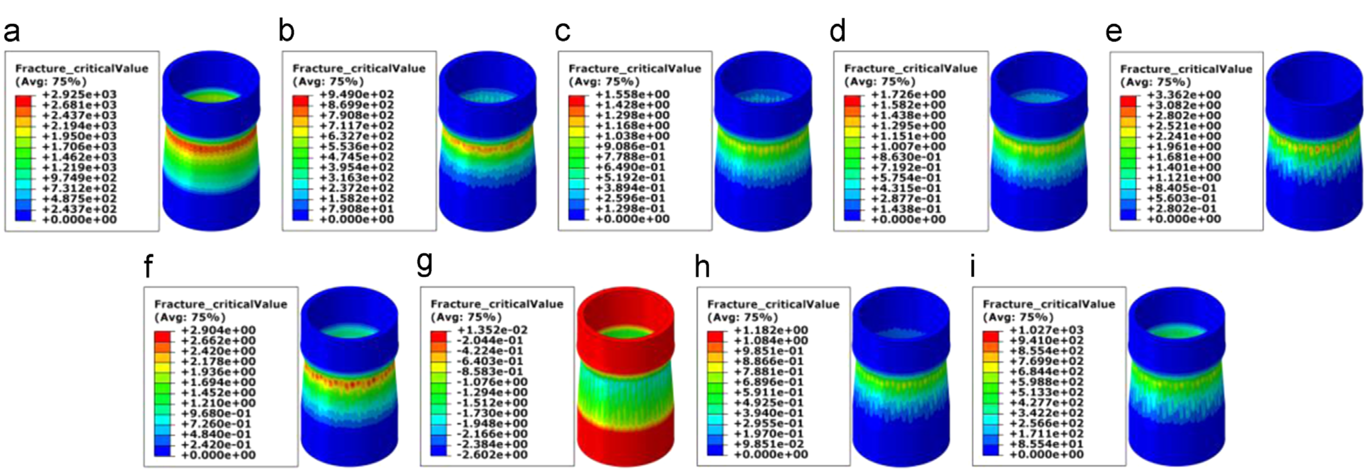

Fig. 7. Distributions of the damage values in the spinnability test with different criteria at fracture moment: (a) Freudenthal model; (b) C–L model; (c) Oh model; (d) Brozzo model; (e) McClintock model; (f) R–T model; (g) Ayada model; (h) Ayada-m model; (i) LeRoy model.

Fig. 9 shows that the maximum damage value predicted by the C–L criterion was always located on the outer layer during the entire spinning process, while the difference between the outer and inner layers was minimal when the thinning rate reached 19%, as shown in Fig. 9b. After that, with increasing thinning rates, the damage values in the second outer layer increased rapidly, and

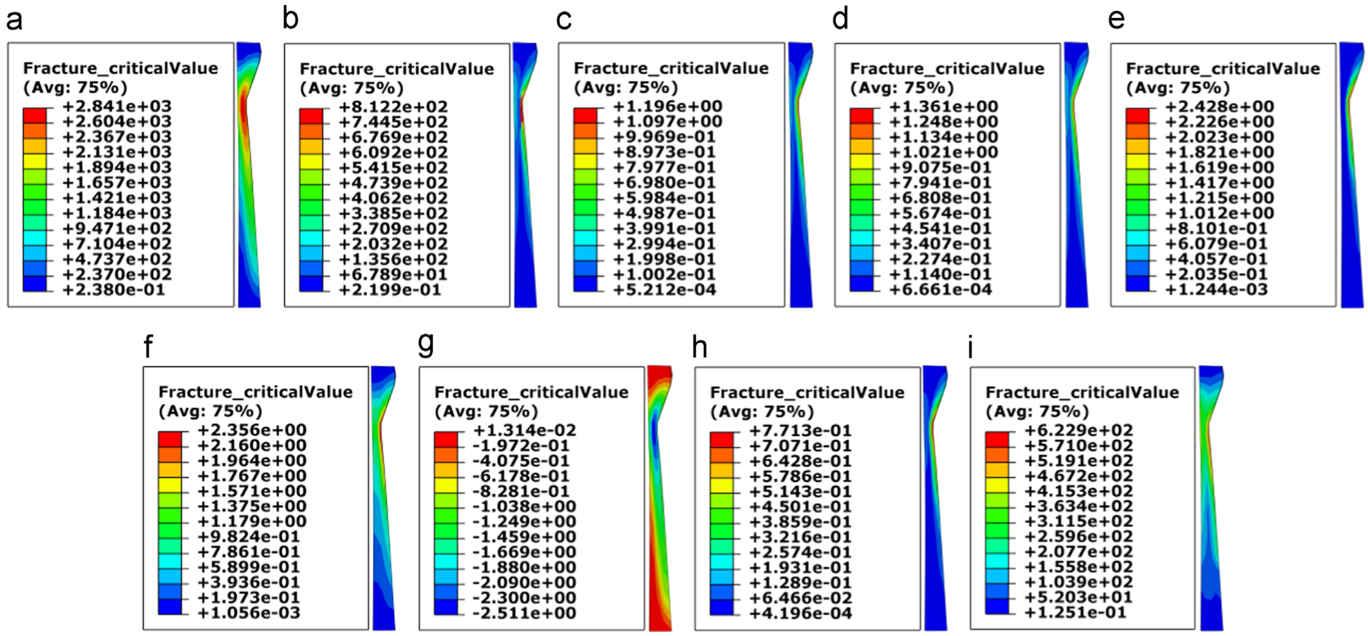

Fig. 8. Distributions of the damage values along thickness direction in the spinnability test with different criteria at fracture moment: (a) Freudenthal model; (b) C–L model; (c) Oh model; (d) Brozzo model; (e) McClintock model; (f) R-T model; (g) Ayada model; (h) Ayada-m model; (i) LeRoy model.

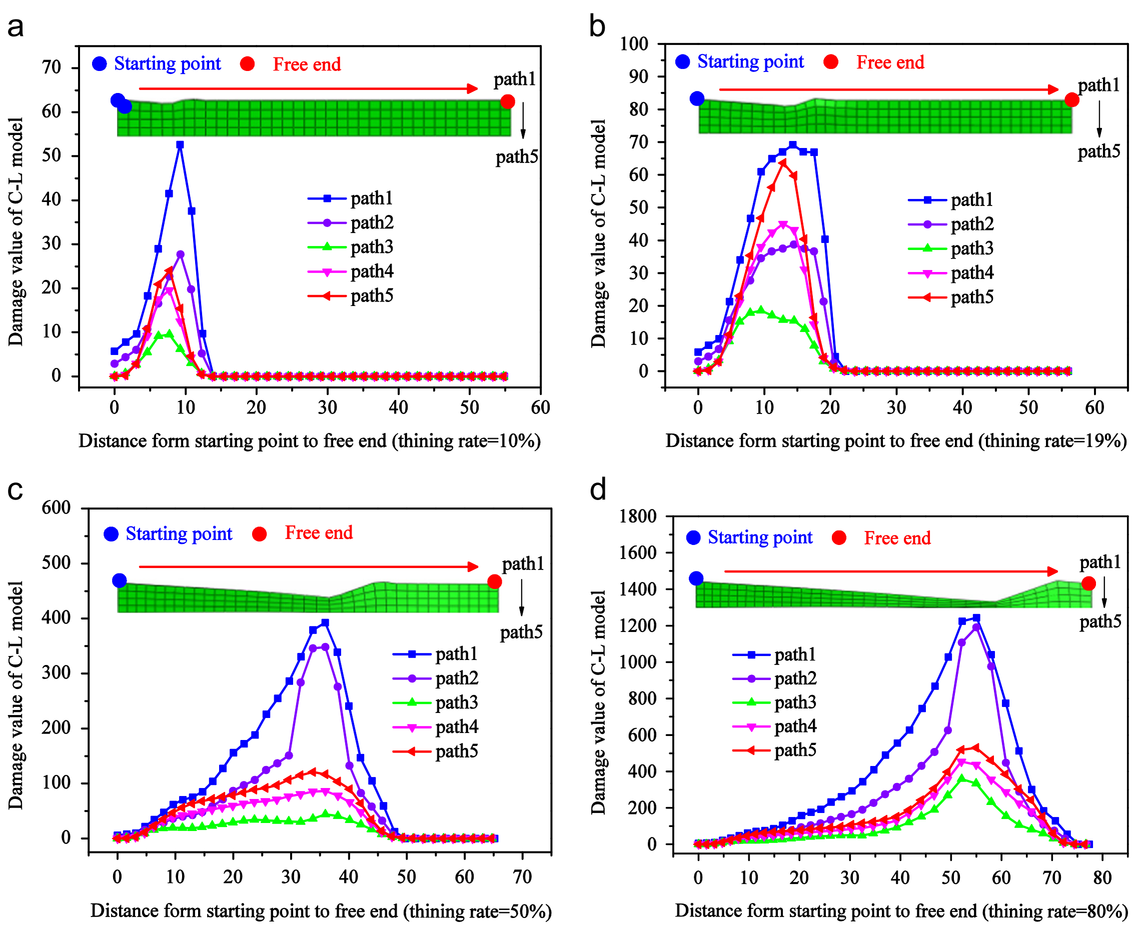

Fig. 9. Damage evaluation in the spinnability test predicted by C–L model: (a) thinning rate = 10%; (b) thinning rate = 20%; (c) thinning rate = 50%; (d) thinning rate = 80%.

gradually exceeded the values of the inner layers, as shown in Fig. 8c and d, indicating that the maximum damage zone gradually moved to outer layers.

Fig. 10 shows the damage evaluation predicted by the R–T model. The damage values decreased progressively along the thickness direction from the outer layer to the inner layer of the

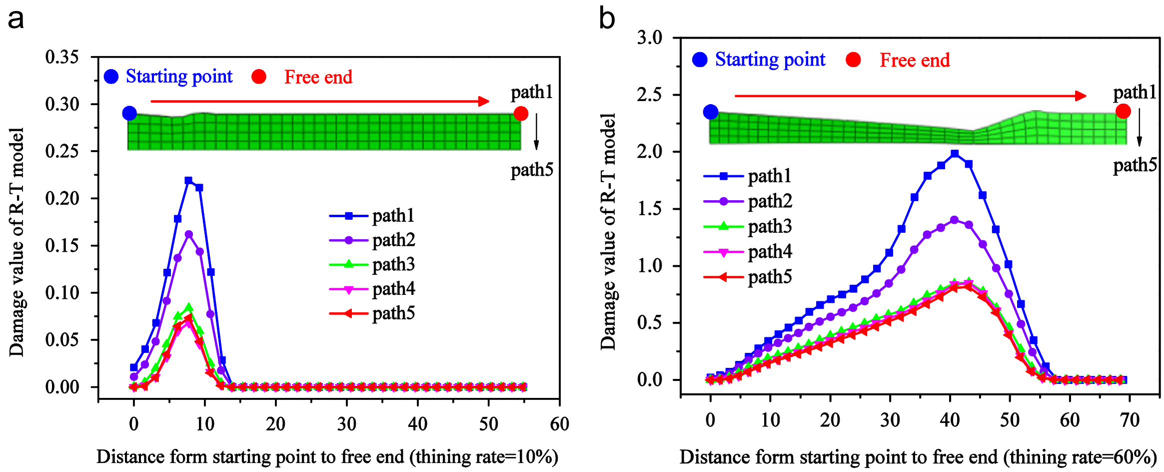

Fig. 10. Damage evaluation in the spinnability test predicted by R–T model: (a) thinning rate = 10%; (b) thinning rate = 60%.

as-spun tube, as shown in Fig. 10a and b. The results predicted by R–T model showed greater damage values in the middle layer than in the inner layer at various thinning rates, indicating that the crack could not occur in the inner layer. However, cracks often occurred on the inner or outer surface of as-spun tubular workpieces in spinning practice. In an experimental study on tube spinning of Ti-15-3 titanium alloy, Shan et al. [36] found that smaller thinning rates induced cracking on the inner surface, while larger thinning rates caused cracking on the outer surface. This phenomenon was also observed in tube spinning of LF6 (5A06) aluminum alloy by Wang [37]. For the C–L model, the middle layer always exhibited the minimum damage value, indicating that no crack could initiate in this layer. Moreover, at lower thinning rates, the damage value accumulated on the inner surface was very closer to that on the outer surface, probably causing crack initiation on the inner surface for materials with lower plasticity and damage limits. To summarize, the predictions obtained with the C–L model were more consistent with practical observations.

5. Discussion

The causes for the fracture mode are mainly known to be the diverse stress states in the forming process, which have important influence on the ductility of the material. To reveal how the aforementioned surface crack initiated in tube spinnability test, the average stress triaxiality introduced by Bao et al. [38] were calculated, which is defined as:

$$\left(\frac{\sigma_m}{\bar{\sigma}}\right)_{av} = \frac{1}{\bar{\varepsilon}_f^p}\int_0^{\bar{\varepsilon}_f^p} \frac{\sigma_m}{\bar{\sigma}} d\bar{\varepsilon}^p \tag{2}$$

Similar to the average stress triaxiality, the average Lode parameter is defined as:

$$(L)_{av} = \frac{1}{\bar{\varepsilon}_f^p}\int_0^{\bar{\varepsilon}_f^p} \left(\frac{2\sigma_2-\sigma_1-\sigma_3}{\sigma_1-\sigma_3}\right) d\bar{\varepsilon}^p \tag{3}$$

However, the changes of the stress components in the spinning process followed a cyclical pattern. To better visualize the change of stress state in the spinnability test, the periodic stress triaxiality and periodic Lode parameter were introduced, defined by

$$\left(\frac{\sigma_m}{\bar{\sigma}}\right)_{periodic} = \frac{1}{\bar{\varepsilon}_{periodic}^p}\int_0^{\bar{\varepsilon}_{periodic}^p} \frac{\sigma_m}{\bar{\sigma}} d\bar{\varepsilon}^p \tag{4}$$

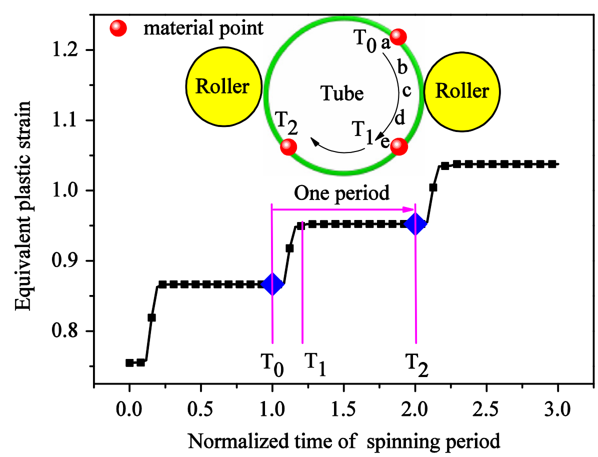

Fig. 11. Definition of one spinning period.

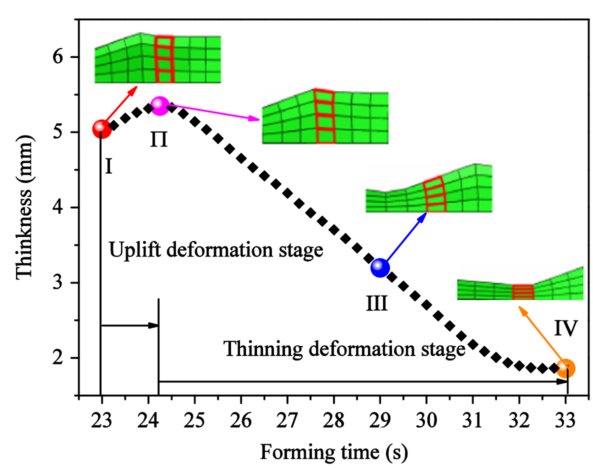

Fig. 12. Changes of thickness for material at fracture location.

$$(L)_{periodic} = \frac{1}{\bar{\varepsilon}_{periodic}^p}\int_0^{\bar{\varepsilon}_{periodic}^p} \left(\frac{2\sigma_2-\sigma_1-\sigma_3}{\sigma_1-\sigma_3}\right) d\bar{\varepsilon}^p \tag{5}$$

where $\bar{\varepsilon}_{periodic}^p$ is the accumulation of equivalent plastic strain during one feeding cycle of the roller, as shown in Fig. 11. When the material point rotated close to the roller (at T_0 moment), the equivalent plastic strain started to increase rapidly until the material point passed over the roller beyond a certain distance

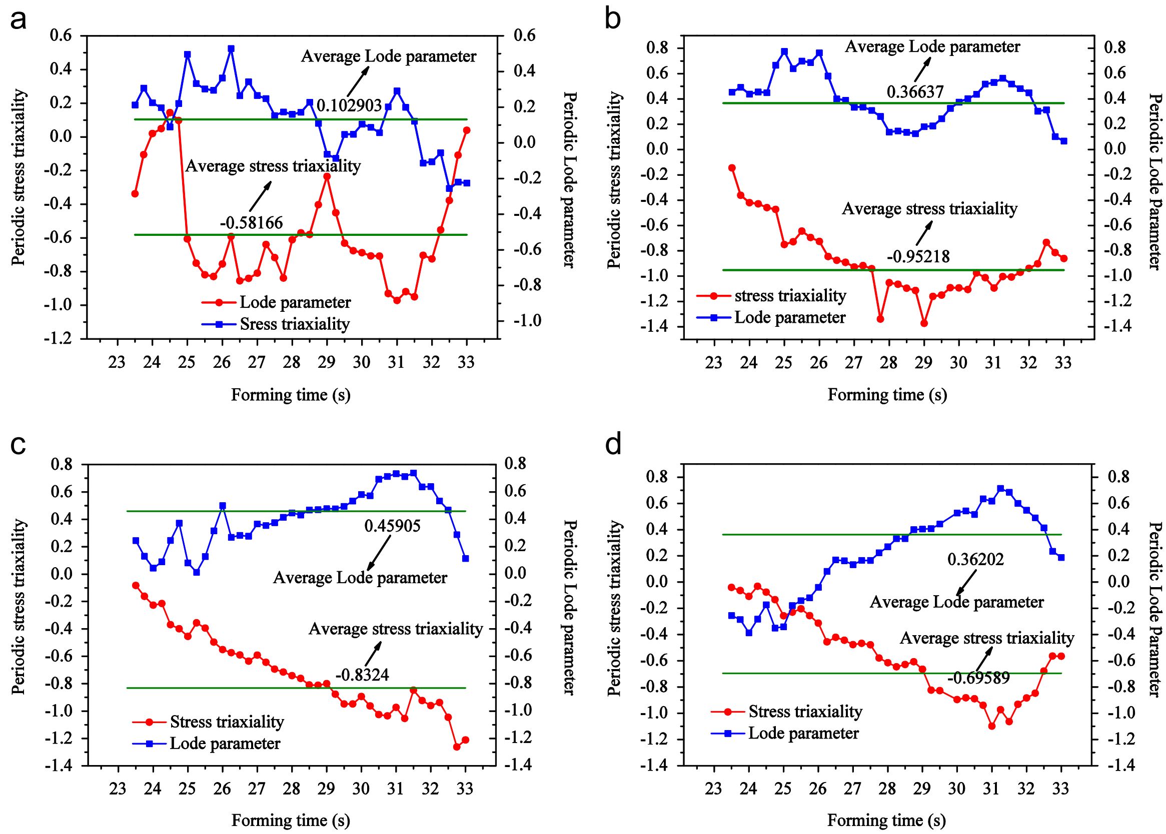

Fig. 13. Changes of periodic stress triaxiality and periodic Lode parameter with spinning process for elements at fracture location: (a) element in the outer layer; (b) element in the second outer layer; (c) element in the second inner layer; (d) element in the inner layer.

(at T_1 moment). Afterwards, no accumulation of the equivalent plastic strain proceeded until it moved approaching the next roller (at T_2 moment). Therefore, half a rational cycle (T_0–T_2) was defined as a spinning period due to the two-roller spinning mode in the present study.

At fracture location, four elements along the thickness direction were selected to analyze their changes in stress states. Since tube spinning was a continuously local forming process and plastic deformation produced primarily in the local zone touched by the roller, the elements at fracture location underwent plastic deformation only when the roller advanced to a certain distance from them. The thickness of the selected elements experienced remarkable changes in the certain spinning period, as shown in Fig. 12. In the uplift deformation stage, as the roller moved close to the elements, the metal piled up in front of the roller, leading to increasing of thickness of the elements. In the thinning deformation stage, as the roller compressed on the elements, the thickness decreased almost linearly until the failure initiated.

Fig. 13 shows the evolution of the periodic stress triaxiality and periodic Lode parameter for those elements. There were various peaks in the periodic stress triaxiality for outer layer, wherein three most obvious peaks appeared on the end of the uplift deformation stage, the middle of thinning deformation stage, and fracture moment respectively (as shown in Fig. 11, the moment of II, III and IV represented). Meanwhile, the periodic Lode parameter took on contrary changes during the spinning process. Fig. 13b, c and d shows that the periodic stress triaxiality of other layers decreased gradually in the early stage and then varied within a lower range. It is worthy to note that the periodic stress triaxiality for middle layers was always negative, while the periodic Lode parameter was always positive throughout the entire spinning deformation process, indicating compression deformation mainly occurred on the middle layers.

The stress states in the forms of the periodic Lode parameter and periodic stress triaxiality collected from the fracture location of the tube are shown in Fig. 14. In view of stress distribution in radial, circumferential and axial directions, the deformation characteristics (modes) in the tube spinnability test were analyzed, which ideally leads to a prediction of potential damage in the formed work pieces.

At the uplift deformation stage, the metal built up in front of the roller, producing tensile radial, tensile tangential and compressive axial stresses on the outer layer. Meanwhile, the stress state with one tensile and two compressive stresses dominated the uplift deformation stage for other layers.

When the deformation proceeded into the thinning stage, triaxial compressive stresses were generated immediately on the outer and second outer layers. While for the inner and the second inner layers, the material experienced a transition stage (as shown in Fig. 14c and d) before entering the triaxial compression zone. In the middle and final thinning stage, the outer layer exhibited a stress state with one tensile and two compressive stresses, while the other layers yet experienced triaxial compression.

It is worthy to note that the outer layer was located at the highest position in the space of the Lode parameter and stress triaxiality at fracture moment, followed by the inner layer, and the middle layers, lowest. Likewise, in the view of the average stress triaxiality, the outer layer also stayed at the highest position in the aforementioned space. Therefore, the middle layers possessed higher plasticity due to higher hydrostatic pressure [39,40], while the outer layer was prone to fracture firstly.

For all the layers, the triaxial compressive stress state dominated the thinning deformation; however, there was great difference among them. Thus, a typical period in the thinning deformation stage was selected to show the discrepancy. Fig. 15a shows the changes of the equivalent plastic strain and the stress

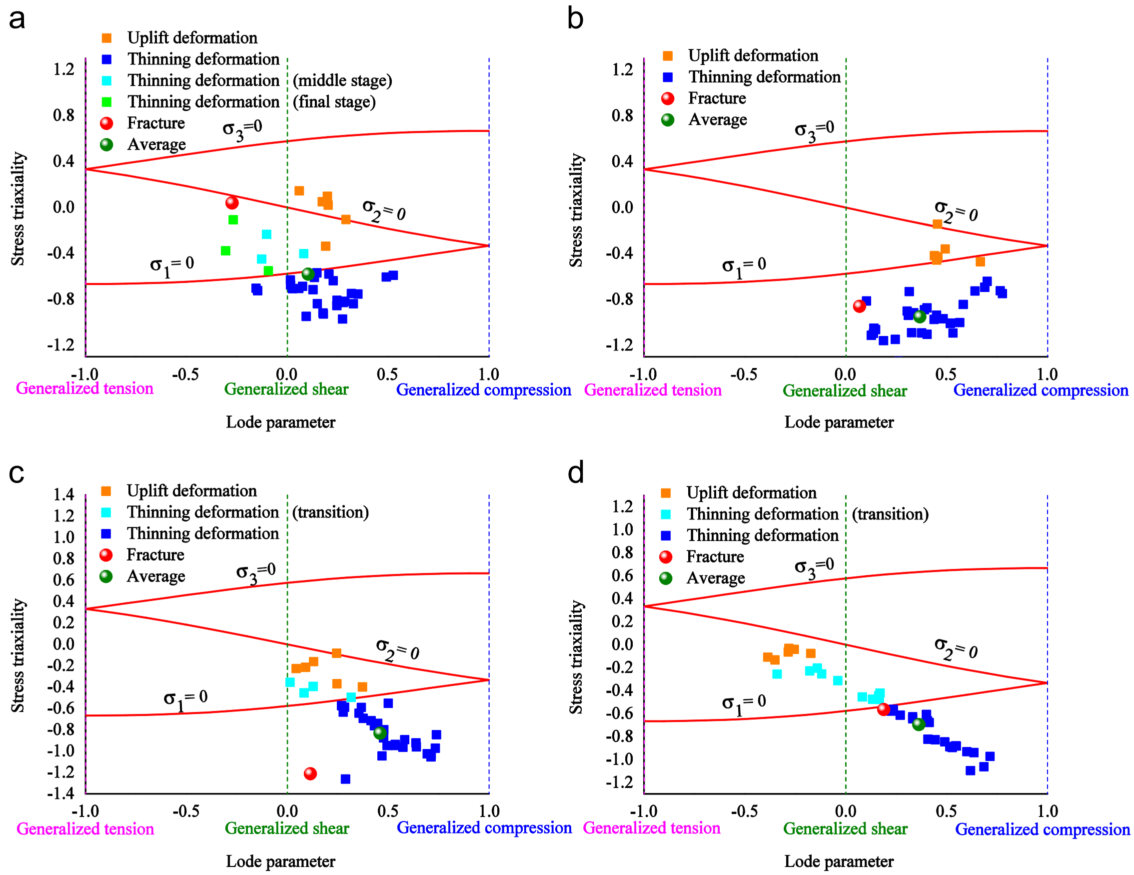

Fig. 14. The $\left((\sigma_m/\bar{\sigma})_{\text{period}}, (L)_{\text{period}}\right)$ space for elements at fracture location: (a) element in the outer layer; (b) element in the second outer layer; (c) element in the second inner layer; (d) element in the inner layer.

triaxiality in the selected period for the outer layer. In a time interval between T_0 and T_1 from Point *a* to *e* (as shown in Fig. 10), drastic changes appeared in the stress triaxiality, and the equivalent strain increased remarkably. Therefore, we focused our discussion on this time interval in the selected period, the discrepancy of different layers is shown in Fig. 15b. At the midpoint (Point c), all of the layers were subjected to triaxial compressive stresses. While for other points, great differences existed in these layers, especially for the outer and the second outer layers.

When the material point rotated close to the roller, higher tensile axial stress started to develop in outer layer, and achieved maximum value before the midpoint, while the tensile tangential stress decreased to the minimum value at midpoint, as shown in Fig. 15c and d. As the material point passed the midpoint, the triaxial compression finally transformed into the stress state at Point e, shown as tensile axial, tensile tangential and compressive radial stresses. The same situation also occurred in other layers for the tensile axial stress before the midpoint, but when the material point passed the midpoint, both compressive axial and tangential stresses were generated. Moreover, the second outer layer was always subjected to the triaxial compressive stresses after the midpoint in the selected period.

In addition, the deformation characteristics for outer-layer element were analyzed since this is a critical location for crack initiation in the spinning process. At the middle point (Point c), the stress state of the outer layer was much closer to that of upsetting deformation. For other points (especially for Point *b* and *d* at which the equivalent strain increased remarkably), the stress state of the outer layer was similar to that of tensile deformation. At Point e, although the Lode parameter was nearly zero, the stress triaxiality exhibited a greater positive value, which cannot be appropriately treated as a pure shear stress state [41]. Tensile and upsetting tests thus were used as benchmark tests for the tube spinnability test, because the similar deformation history between the mechanical test and the applied forming process yielded greater predictive accuracy [42].

This situation not only occurred in this selected period, but also continued in the entire thinning deforming stage. The axial and tangential stresses collected from Point b and e for different layers are shown in Fig. 16. It is noted that, in the middle of thinning deformation stage and fracture moment (as shown in Fig. 12, the moment of III and IV represented), both the axial and tangential stresses reached a higher value for the outer layer, leading to peak values of the stress triaxiality as shown in Fig. 13a, thus exhibiting a stress state with one tensile and two compressive stresses, as shown in Fig. 14a. In addition, no matter for inner or outer layers, higher tensile axial stresses produced at the material point when it rotated close to the roller (at Point b). In case of microcrack initiated at the material point, a circumferential crack was prone to develop from there due to higher tensile axial stress occurring periodically in the thinning deformation stage.

To be able to realize proper failure prediction, the DFCs should thus capture the fracture mechanism by considering the governing rules of the vital factors such as the equivalent plastic strain, the first tensile principal stress, or the stress triaxiality in their formulations either explicitly or implicitly.

In view of the stress/strain-driven ductile damage evolution mechanisms under large deformation, the equivalent plastic strain was considered to be associated with the deformation level and void nucleation [17]. All of the ductile fracture criteria selected in this research (other than the Ayada model) showed that the

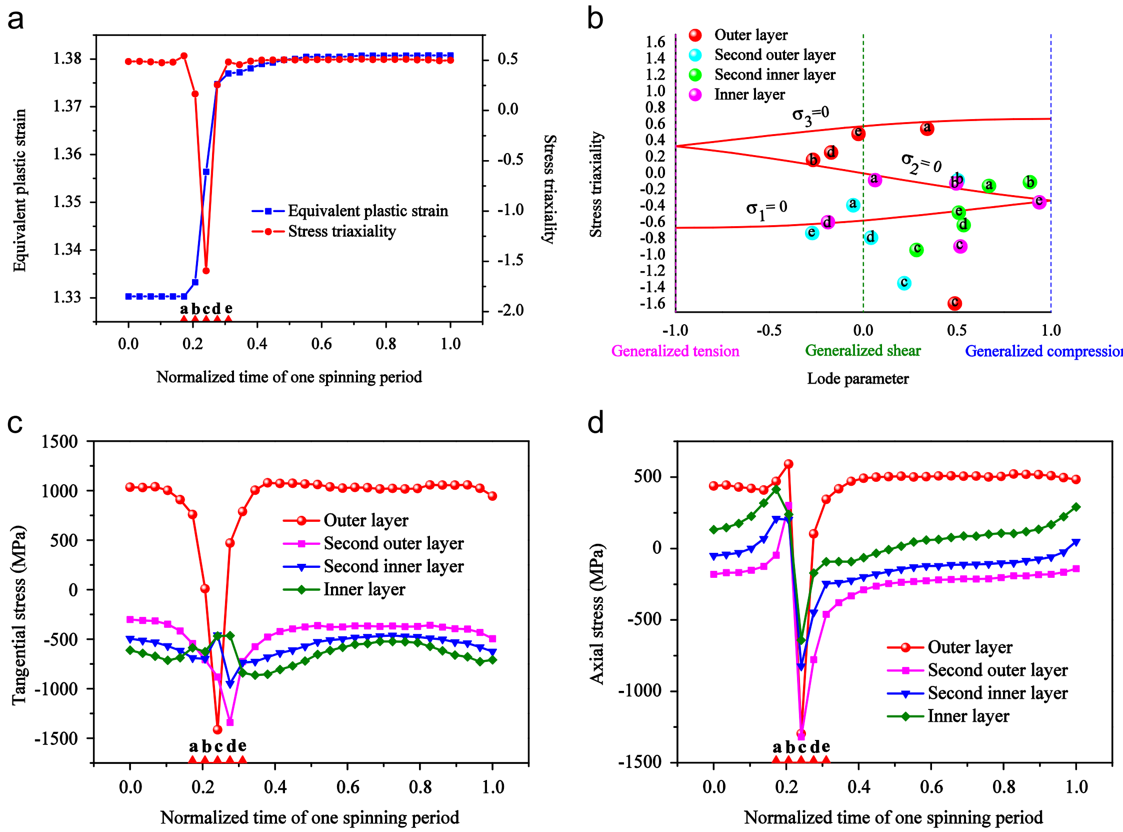

Fig. 15. (a) changes of the stress triaxiality and equivalent plastic strain in the selected period for element on outer layer at fracture location; (b) the $(\sigma_m/\bar{\sigma}, L)$ space of time points in the selected period for elements at fracture location; (c) changes of tangential stress in the selected period for elements at fracture location; (d) changes of axial stress in the selected period for elements at fracture location.

damage values at the outer layer increased monotonically with equivalent plastic strain. This behavior was consistent with the observation that the likelihood of ductile fracture increased with increasing plastic deformation, as shown in Fig. 17. The failure of Ayada model can be explained by the variation of stress triaxiality in the selected period, as shown in Fig. 15. At the midpoint, the stress triaxiality reached the minimum negative value due to the compression action of the rollers. Simultaneously, the equivalent plastic strain increased sharply, causing the damage value to decrease with increasing plastic deformation.

After comparing damage values from the tube spinnability test with the damage limits obtained by the tensile and upsetting tests, the spinnability predicted by the selected criteria are shown in Fig. 18. For all of the DFCs considered, the C–L criterion based on the damage limit obtained by the tensile test provided a satisfactory prediction on the spinnability of TA2 titanium tube, which was only 9% less than the measured experimental value, as shown in Fig. 18a.

In addition, only four criteria, i.e. the C–L, Oh, Brozzo and Ayada-m models could predict the spinnability based on both tensile and upsetting tests. However, it is clear that the spinnability for TA2 titanium obtained by the tensile and upsetting tests differed evidently for those criteria and the maximum difference in the spinnability obtained by the selected tests was 35% for the Ayada-m criterion. This discrepancy may depend on how the DFCs captured the fracture mechanism by considering the governing rules of the vital factors in their formulations.

In the stress/strain-driven ductile damage evolution mechanisms under large deformation, the growth of microvoids was driven only by the first principal tensile stress [23,30]. When the first principal stress was negative and therefore the material experienced triaxial compression, the microvoids were not able to grow continuously. As reported in [43,44], the first principal tensile stress was taken as the cut-off value of $(L-3)/(3\sqrt{L^2+3})$ for the stress triaxiality by Cockcroft and Latham [27], Oh et al. [28], Brozzo et al. [29], and LeRoy et al. [34]. Similarly, the second principal tensile stress was also regarded as a threshold value for the stress triaxiality in the McClintock model. For the Ayada-m model, a cut-off value of $-1/3$ for the stress triaxiality was coupled into the formulation. Therefore, the changes of stress triaxiality with different cut-off values were discussed in the tensile, upsetting and tube spinnability test, as shown in Fig. 19. Compared with the upsetting test, the variation of stress triaxiality in the tensile test was much closer to that in the spinnability test throughout the entire forming process with both cut-off values. Moreover, the stress triaxiality in Ayada-m model with the cut-off value of $-1/3$ exhibited almost no intersection between the spinnability and upsetting tests, resulting in a much lower prediction of the spinnability performed by the upsetting test.

Assuming that the damage limit obtained by the spinnability test equals one, the damage evolution with normalized displacement for the tensile, upsetting, and spinnability tests are shown in Fig. 20. For these models, the spinnability test exhibited the maximum damage limit, while the tensile test was second, and the upsetting test, third. In the uniform deformation stage of tensile test, the damage value predicted by these models showed little difference with that in the upsetting test. When necking deformation took place, the damage value in the tensile test increased remarkably, finally reached a higher damage limit than the upsetting test, which more approached the damage limit in the spinnability test.

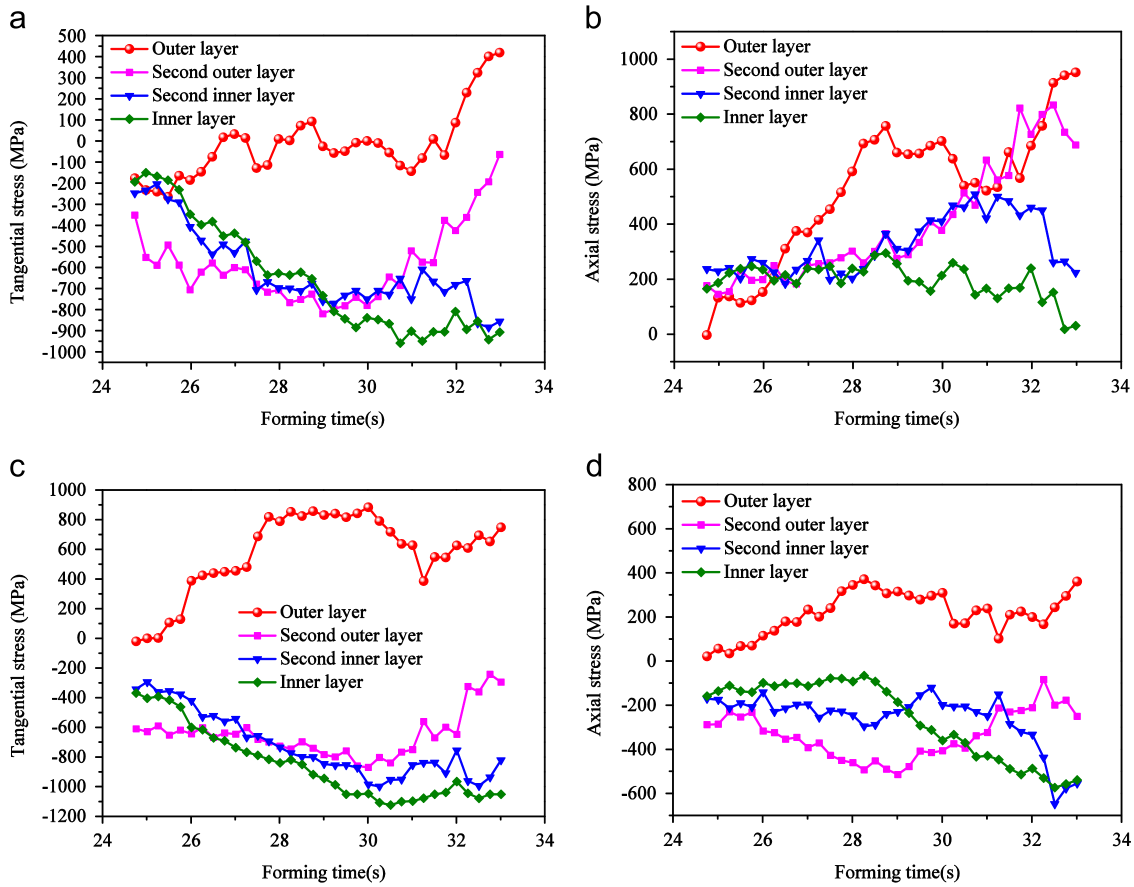

Fig. 16. Changes of stress components with thinning deformation for elements at fracture location: (a) tangential stress collected from point b; (b) axial stress collected from point b; (c) tangential stress collected from point e; (d) axial stress collected from point e.

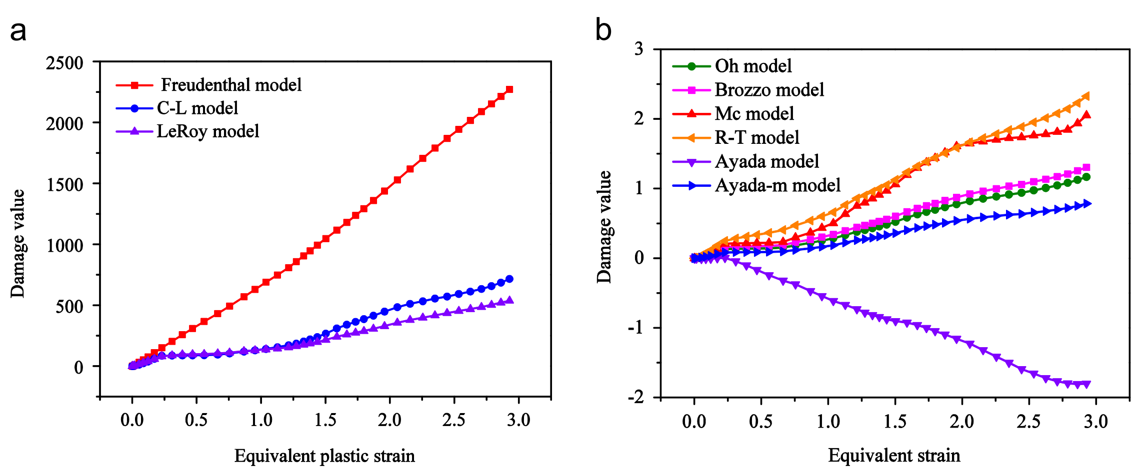

Fig. 17. Damage values against the equivalent plastic strain in the spinnability test with different criteria: (a) Predicted by Freudenthal, C–L and LeRoy models; (b) Predicted by other models selected in our research.

6. Conclusions

1) The periodic stress triaxiality and periodic Lode parameter were calculated for the elements on different layers at fracture location. The results showed that the middle layers possessed higher plasticity due to higher hydrostatic pressure in the spinnability test, while the outer layer was prone to fracture firstly.
2) In each spinning period, high tensile axial stress generated at the material point which rotated close to the roller, indicating that once microcrack initiated at the material point, a circumferential crack was prone to develop from there due to high tensile axial stress occurring periodically in the thinning deformation stage.
3) The constant cut-off value of stress triaxiality was incorporated into the Adaya model. The modified Ayada model provided reasonable predictions of ductile fracture in tube spinnability tests as well as tensile and upsetting tests.
4) All of the selected ductile fracture criteria were able to predict fracture initialization and location correctly in tensile tests due to the localized necking deformation, which made it easily to capture the failure for those criteria. For the upsetting test,

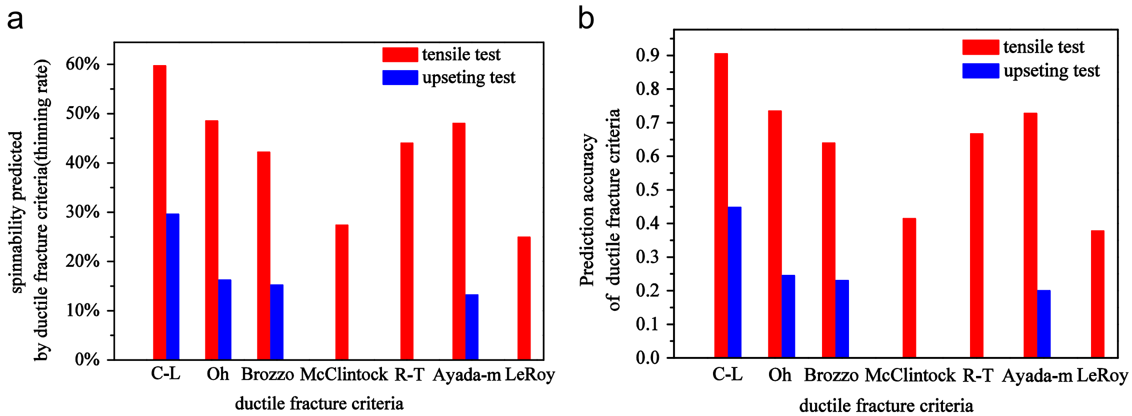

Fig. 18. Spinnability predicted by tensile and upsetting tests with different criteria: (a) predicted spinnablity; (b) prediction accuracy.

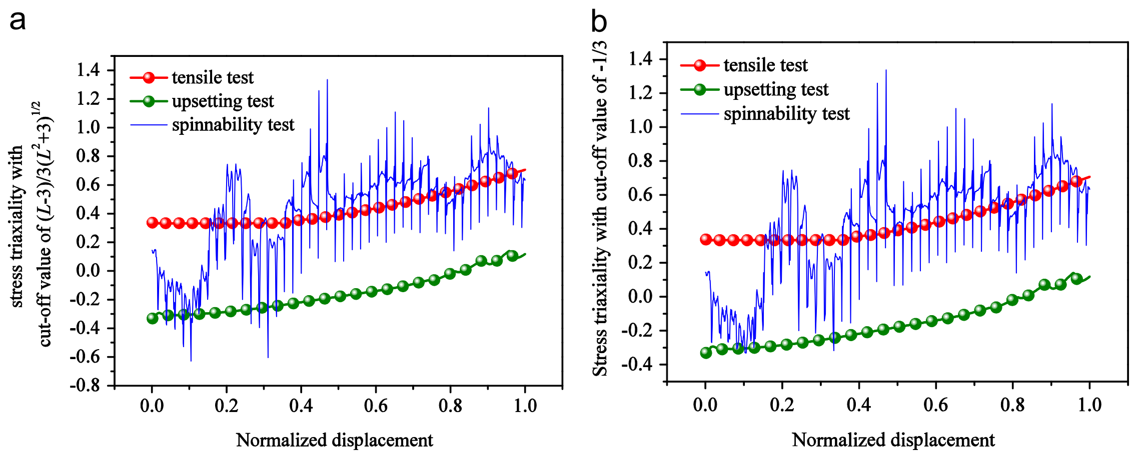

Fig. 19. Changes of stress triaxiality with deformation process for tensile, upsetting and spinnability tests: (a) with cut-off value of $(L-3)/(3\sqrt{L^2+3})$; (b) with cut-off value of $-1/3$.

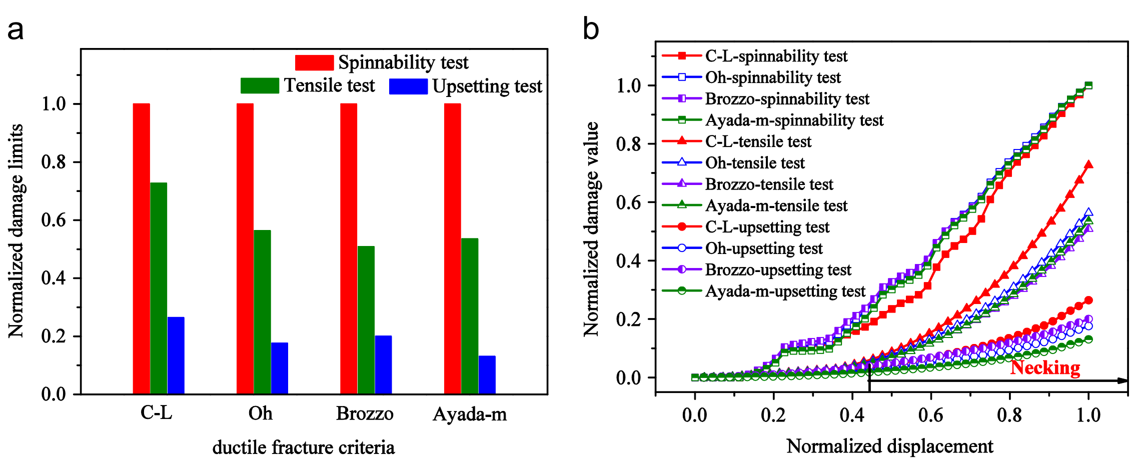

Fig. 20. Values for tensile, upsetting and spinnability tests: (a) normalized damage limits; (b) normalized damage values.

those DFCs based on micro-void analysis, such as McClintock, R–T and LeRoy models, could not predict the fracture behavior, while only the C–L, Oh, Brozzo and the modified Ayada criteria were able to predict the damage location.

5) Except for the Freudenthal, R–T and Ayada models, the other six ductile fracture criteria correctly predicted the damage distribution on TA2 titanium tubes in spinnability tests, while the C–L criterion provided the highest prediction accuracy on the spinnability of TA2 titanium tube, which was only 9% less than the measured experimental value.
6) Compared with the upsetting test, the variation of stress triaxiality in the tensile test was much closer to that in the spinnability test for both cut-off values coupled into the C–L and Ayada-m models respectively, which led to higher prediction accuracy on the spinnability of TA2 titanium by the tensile test.

Acknowledgment

This work was supported by the National Natural Science Foundation of China (Nos. 51275131 and 50705019), authors would like to appreciate Dr. Brian Casey, Senior Software Engineer of MSC Software Nastran Development, for the time he has spent and his important suggestions on proof-reading the manuscript.

References

[1] Wong CC, Dean TA, Lin J. A review of spinning, shear forming and flow forming processes. Int J Mach Tools Manuf 2003;43(14):1419–35.
[2] Music O, Allwood JM, Kawai K. A review of the mechanics of metal spinning. J Mater Process Technol 2010;210(1):3–23.
[3] Xu Y, Zhang SH, Li P, Yang K, Shan DB, Lu Y. 3D rigid-plastic FEM numerical simulation on tube spinning. J Mater Process Technol 2001;113:710–3.
[4] Shan DB, Lu Y, Li P, Xu Y. Experimental study on process of cold-power spinning of Ti–15–3 alloy. J Mater Process Technol 2001;115(3):380–3.
[5] Gur M, Tirosh J. Plastic flow instability under compressive loading during shear spinning process. Trans ASME J Eng Ind 1982;104:17–22.
[6] Jahazi M, Ebrahimi G. The influence of flow-forming parameters and microstructure on the quality of a D6ac steel. J Mater Process Technol 2000;103:362–6.
[7] Ma ZE. Optimal angle of attack in tube spinning. J Mater Process Technol 1993;37:217–24.
[8] Rajnish P, Singhal RP. Shear spinning of technology for the manufacture of long thin wall tubes of small bore. J Mater Process Technol 1995;54:186–92.
[9] Kalpakcioglu S. Maximum reduction in power spinning of tubes. Trans ASME J Eng Ind 1964;86:49–54.
[10] Hill R. On discontinuous plastic states, with special reference to localized necking in thin sheets. J Mech Phys Solids 1952;1(1):19–30.
[11] Swift HW. Plastic instability under plane stress. J Mech Phys Solids 1952;1(1):1–18.
[12] Marciniak Z, Kuczynski K. Limit strains in the processes of stretch-forming sheet metal. Int J Mech Sci 1967;9:609–20.
[13] Stören S, Rice JR. Localized necking in thin sheets. J Mech Phys Solids 1975;23:421–41.
[14] Hora P, Tong L, Reissner J. A prediction method for ductile sheet metal failure in FE-simulation. In: Proceedings of the numisheet'96 conference, vol. 1; 1996. p. 252–6.
[15] Zhu X, Weinmann K, Chandra A. A unified bifurcation analysis of sheet metal forming limits. J Eng Mater Technol 2001;123:329–33.
[16] Zhan M, Gu CG, Jiang ZQ, Hu LJ, Yang H. Application of ductile fracture criteria in spin-forming and tube-bending processes. Comput Mater Sci 2009;47:353–65.
[17] Gurson AL. Continuum theory of ductile rupture by void nucleation and growth. Part I: yield criteria and flow rules for porous ductile media. J Eng Mater Technol 1977;99:2–15.
[18] Tvergaard V, Needleman A. Analysis of the cup-cone fracture in a round tensile bar. Acta Metall 1984;32(1):157–69.
[19] Xue L. Constitutive modeling of void shearing effect in ductile fracture of porous materials. Eng Fract Mech 2008;75(11):3343–66.
[20] Nahshon K, Hutchinson JW. Modification of the Gurson model for shear failure. Eur J Mech A: Solids 2008;27(1):1–17.
[21] Nielsen KL, Tvergaard V. Ductile shear failure or plug failure of spot welds modeled by modified Gurson model. Eng Fract Mech 2010;77(7):1031–47.
[22] Lou YS, Huh H. Prediction of ductile fracture for advanced high strength steel with a new criterion: experiments and simulation. J Mater Process Technol 2013;213(8):1284–302.
[23] Li H, Fu MW, Lu J, Yang H. Ductile fracture: experiments and computations. Int J Plast 2011;27(2):147–80.
[24] Lemaitre J. A continuous damage mechanics model for ductile fracture. J Eng Mater Technol 1985;107:83–9.
[25] Khan AS, Liu HW. A new approach for ductile fracture prediction on Al 2024–T351 alloy. Int J Plast 2012;35:1–12.
[26] Freudenthal FA. The Inelastic Behavior of Solids. New York: Wiley; 1950.
[27] Cockroft MG, Latham DJ. Ductile and workability of metals. J Inst Met 1968;96:33–9.
[28] Oh SI, Chen CC, Kobayashi S. Ductile fracture in axisymmetric extrusion and drawing: Part 2, workability in extrusion and drawing. Trans ASME J Eng Ind 1979;101:36–44.
[29] Brozzo P, DeLuca B, Rendina R. A new method for the prediction of formability limits in metal sheets. In: Proceedings of the seventh biennial conference of the international deep drawing research group; 1972.
[30] McClintock FA. A criterion for ductile fracture by the growing of holes. J Appl Mech 1968;35:363–71.
[31] Rice JR, Tracey DM. On the ductile enlargement of voids in triaxial stress fields. J Mech Phys Solids 1969;17:201–17.
[32] Ayada M, Higashino T, Mori K. Central bursting in extrusion of inhomogeneous materials. In: Proceedings of the first ICTP, adv. technology of plasticity, vol. 1; 1984. p. 553–8.
[33] Bao YB, Wierzbicki T. On the cut-off value of negative triaxiality for fracture. Eng Fract Mech 2005;72(7):1049–69.
[34] LeRoy G, Embury J, Edwards G, Ashby MF. A model of ductile fracture based on the nucleation and growth of voids. Acta Metall 1981;29(7):1509–22.
[35] Bao YB. Prediction of ductile crack formation in uncracked bodies [Ph.D. thesis]. USA: Massachusetts Institute of Technology, 2003. p. 62–64.
[36] Shan DB, Tong WZ, Xu Y, Lu Y. Effects of plastic deformation inhomogeneity on process of cold power spinning of Ti-15-3. Chin J Nonferrous Met 2000;10(6):887–90 (in Chinese).
[37] Wang BX, Lu XY, Zhang SH. Analysis of tube cracks of LF6 alloy in flow turning. Forg Stamp Technol 2005:79–82 (in Chinese).
[38] Bao YB, Wierzbicki T. On fracture locus in the equivalent strain and stress triaxiality space. Int J Mech Sci 2004;46(1):81–98.
[39] Wang ZR. Physical essence of lode parameter and its effect on plastic flow. Acta Mech Solida Sin 2006;27(3):277–82.
[40] Cui XL, Wang XS, Yuan SJ. Experimental verification of the influence of normal stress on the formability of thin-walled 5A02 aluminum alloy tubes. Int J Mech Sci 2014;88:232–43.
[41] Bai YL, Wierzbicki T. A new model of metal plasticity and fracture with pressure and Lode dependence. Int J Plast 2008;24:1071–96.
[42] Goijaerts AM, Govaert LE. Evaluation of ductile fracture model for different metals in blanking. J Mater Process Technol 2001;110(3):312–23.
[43] Lou YS, Yoon JW, Huh H. Modeling of shear ductile fracture considering a changeable cut-off value for stress triaxiality. Int J Plast 2014;54:56–80.
[44] Lou YS, Huh H. Evaluation of ductile fracture criteria in a general three-dimensional stress state considering the stress triaxiality and the lode parameter. Acta Mech Solida Sin 2013;26(6):642–58.